nature materials

Article

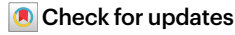
https://doi.org/10.1038/s41563-023-01663-5

Forensics of polymer networks

Received: 9 August 2022

Accepted: 11 August 2023

Published online: 25 September 2023



Andrey V. Dobrynin ® ¹ ⋈, Yuan Tian ® ¹, Michael Jacobs¹, Evgeniia A. Nikitina ® ², Dimitri A. Ivanov ® ².³, Mitchell Maw¹, Foad Vashahi ® ¹ & Sergei S. Sheiko ® ¹ ⋈

Our lives cannot be imagined without polymer networks, which range widely, from synthetic rubber to biological tissues. Their properties elasticity, strain-stiffening and stretchability—are controlled by a convolution of chemical composition, strand conformation and network topology. Yet, since the discovery of rubber vulcanization by Charles Goodyear in 1839, the internal organization of networks has remained a sealed 'black box'. While many studies show how network properties respond to topology variation, no method currently exists that would allow the decoding of the network structure from its properties. We address this problem by analysing networks' nonlinear responses to deformation to quantify their crosslink density, strand flexibility and fraction of stress-supporting strands. The decoded structural information enables the quality control of network synthesis, comparison of targeted to actual architecture and network classification according to the effectiveness of stress distribution. The developed forensic approach is a vital step in future implementation of artificial intelligence principles for soft matter design.

The topology of polymer networks is an ill-defined product of erratic node formation processes. Any reasonable efforts to project the network architecture by specifying stoichiometry and the synthetic pathway are instantly scrambled by the swift scaffold percolation generating a stochastic distribution of structural elements (Fig. 1a)¹⁻⁴. The problem is further exacerbated by the limited ability of traditional characterization techniques to isolate and measure contributions from the individual building blocks within an interconnected construct (Fig. 1b)⁵. Even the seemingly trivial parameters such as actual crosslink density and functionality are unknown. There are two general approaches, both imperative, to uncover network organization. The so-called structure-to-property approach employs model networks with synthetically predefined strands, loops and dangles to quantify the contributions of each element to a specific property, for example, the modulus⁶⁻⁸. Although informative, this method is unsuitable for ordinary polymer networks with unknown topology. Alternatively, a structure-from-property approach allows the extraction of structural information. Over the years, the elastic modulus or equilibrium swelling ratio have been used for evaluating the crosslink density 1,2 . Recently a step forward in model network characterization was made by applying a double-quantum low-field NMR in combination with equilibrium swelling experiments to assess the network strand degree of polymerization and a defect weight fraction by using the Flory–Rehner model of swollen phantom networks and Miller–Macosko theory of gelation 9 . However, this approach ignores contributions from entanglements and loops in the network elastic response and is very sensitive to minute changes in the Flory–Huggins parameter 10 .

We address this problem by developing a facile methodology for deciphering the network structure from its nonlinear response to deformation (Fig. 1c). Unlike the traditional analysis of a single data point, for example, the modulus at small deformations ^{1,2,4,8}, we analyse the entire shape of a stress–strain curve, containing information about the network structure. By expanding the analysis to multiple self-similar networks, we use their cross-correlated mechanical response to quantify the strand Kuhn length, density of stress-supporting strands, onset of entanglement-defined elasticity and, in some cases, effective cross-link functionality and loop contributions. Our approach can be viewed

¹Department of Chemistry, University of North Carolina at Chapel Hill, Chapel Hill, NC, USA. ²Department of Chemistry, Lomonosov Moscow State University, Moscow, Russia. ³Institut de Sciences des Matériaux de Mulhouse (IS2M), CNRS UMR 7361, Université de Haute-Alsace, Mulhouse, France. © e-mail: avd@email.unc.edu; sergei@email.unc.edu

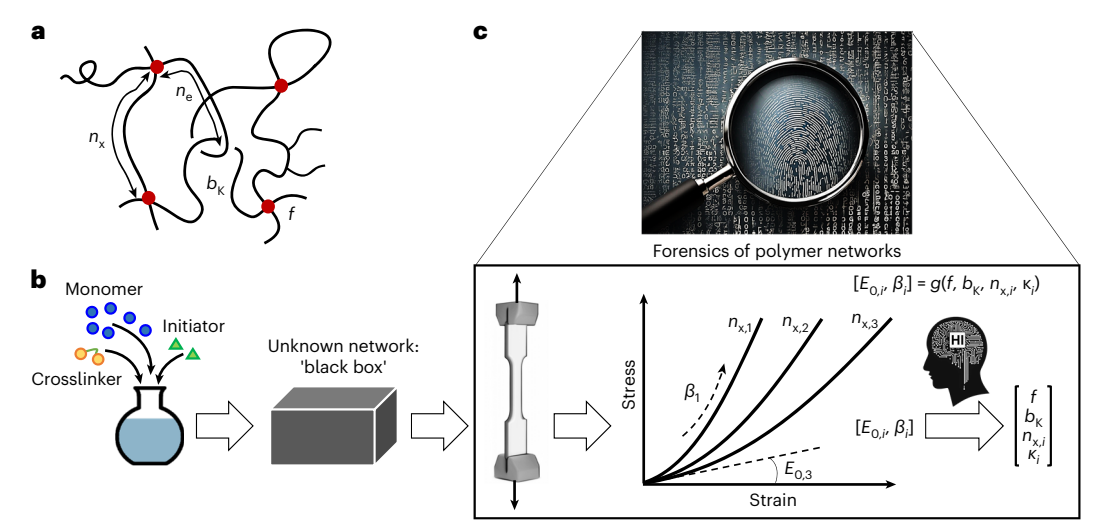


Fig. 1| **Forensics methodology. a**, Schematic of a real polymer network (containing various defects such as loops, multiple strands, side chains and dangles) defined by a set of structural parameters: degree of polymerization between crosslinks (red dots), n_x and entanglements, n_e : crosslink functionality, f; and the Kuhn length of a network strand, b_K . **b**, Synthesis of a series of self-similar networks with different crosslink densities and unknown internal

organization (black box). **c**, Forensics procedure includes deformation test to record nonlinear stress–strain curves characterized by the Young's modulus, $E_{0,i}$ and strain-stiffening parameter, β_i , and deciphering network structure from the domain of the measured $[E_{0,i},\beta_i]$ combinations to deliver the structural parameters $[f,b_k,n_{x,i},\kappa_i]$ using a theoretical model (Human Intelligence (HI)), where κ_i is the network quality factor defined in the main text.

as a macroscopic analogue of single chain stretching experiments that use large deformations to extract molecular information 11,12 .

The developed methodology does not require any assumptions about the type of structural defects^{8,13}, the mechanism of network assembly^{8,14,15} or about the solvent quality in swelling tests^{1,2} to establish structure-property relationships. Unlike spectroscopic 16 and scattering¹⁷ techniques that involve complex structure-perturbing preparation procedures, our method deals with as-synthesized materials intended for direct use in practical applications. Our approach takes into account contributions from crosslinks, defects (loops and dangling ends) and trapped entanglements (Fig.1a)^{1,13,18} responsible for the elastic modulus at small deformations, E_0 , as well as its strain-stiffening at large deformations due to the finite strand extensibility, β . The only requirement is to have a series of networks with varying crosslink density prepared by the same synthesis protocol. Analysis of a single network is also possible but delivers less information; this information includes the degree of polymerization (DP) of the network strands in weakly entangled networks and whether crosslinks or entanglements control network elasticity.

The developed methodology was validated by applying the forensic approach to a set of basic systems including natural rubber 19, end-crosslinked linear poly(dimethyl siloxane) (PDMS) and brush-like poly(n-butyl acrylate) (PBA) networks with a systematically varied DP of side chains $n_{\rm sc}=0-41$, number of repeat units between them $n_{\rm g}=1-10$ and DP of the backbone between crosslinks $n_{\rm x}=25-1,200$ (refs. 20,21). Since synthetic control of the network topology is limited, we performed coarse-grained molecular dynamics simulations of linear chain and diamond networks that allow accurate variations of strand dimensions, effective crosslinking functionality and defect distribution (Supplementary Information).

We first apply the forensic approach to results of molecular dynamics simulations of phantom networks^{1,22} made by the crosslinking of non-interacting bead–spring chains (precursor chains) with a DP of N=1,025 in a melt state (Supplementary Information). The networks have dangling ends and loops but are without entanglements as network strands are permitted to cross each other. The equation of state for phantom networks undergoing uniaxial elongation, λ , under

true stress, σ_{true} , is derived by considering individual network strands as nonlinear springs of finite extensibility^{3,23}

$$\sigma_{\text{true}}(\lambda) = (\lambda^2 - \lambda^{-1}) \frac{G}{3} \left[1 + 2 \left(1 - \frac{\beta(\lambda^2 + 2\lambda^{-1})}{3} \right)^{-2} \right]$$
 (1)

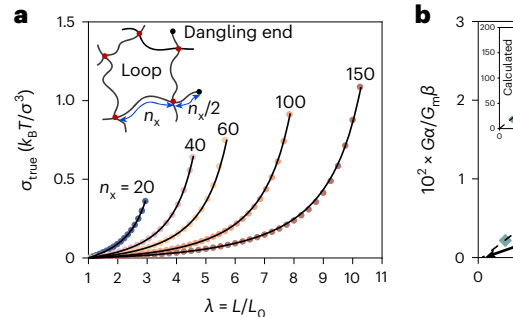
which results in the appearance of the divergent term in the brackets. The strain-stiffening behaviour is defined by the firmness parameter

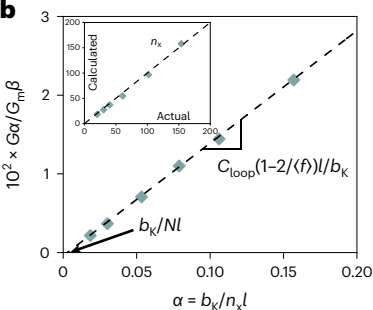
$$\beta \equiv \left\langle R_{\rm in}^2 \right\rangle / R_{\rm max}^2 = \alpha \left(1 - \frac{\alpha}{2} \left(1 - \exp\left(-\frac{2}{\alpha} \right) \right) \right). \tag{2}$$

Equation (2) characterizes the strand extensibility, that is, how much a network strand containing n_x repeat units between crosslinks each with projection length l can be stretched from its initial mean-square end-to-end distance $\langle R_{\rm in}^2 \rangle$ to the fully extended state $R_{\rm max} = n_x l$. The second part of equation (2) expresses β in terms of $\alpha^{-1} = n_x l/b_{\rm K}$, which represents the number of Kuhn segments of length $b_{\rm K}$ per network strand. The structural shear modulus of phantom networks, G, includes contributions from stress-supporting strands between crosslinks with functionality f, dangling ends and loops as

$$G = G_{\rm m} \frac{\langle R_{\rm in}^2 \rangle}{b_{\rm K} R_{\rm max}} \left(1 - \frac{2}{\langle f \rangle} \right) C_{\rm loop} \left(\frac{1}{n_{\rm x}} - \frac{1}{N} \right) \tag{3}$$

where $G_{\rm m}=\rho k_{\rm B}T$ is the monomeric shear modulus defined by the monomer number density ρ and the thermal energy $k_{\rm B}T(k_{\rm B})$, Boltzmann constant; T, absolute temperature). The coefficient $C_{\rm loop}$ describes contribution from loops to G (inset in Fig. 2a), while the factor 1/N quantifies the decrease in the density of stress-supporting strands caused by two dangling ends per precursor chain and having $n_{\rm w}/2$ monomers each (inset in Fig. 2a and Supplementary Information)^{1,2}. The dangling ends reduce the effective crosslink functionality, which is accounted for by using the average value of the crosslink functionality $\langle f \rangle$ (Supplementary Equations (2)–(5)).





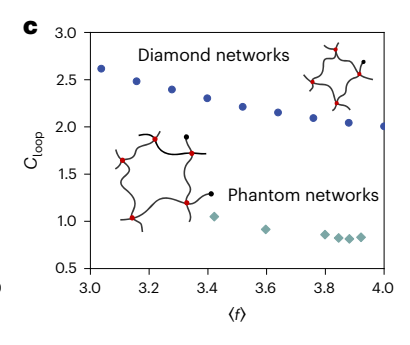


Fig. 2 | **Forensics of phantom networks. a**, Stress—elongation curves obtained by the computer simulation of phantom networks with different crosslink densities made by crosslinking linear bead—spring chains with bead diameter σ and the DP N=1,025, undergoing uniaxial deformation at a constant volume from initial size L_0 to L, described by the elongation ratio $\lambda = L/L_0$. Solid lines are the best fits to equation (1) by considering G and G as fitting parameters (Supplementary Table 1). **b**, The self-similarity of phantom networks of linear chains is confirmed by plotting the reduced shear modulus $\frac{G\alpha}{C_{\rm m}\beta}$ as a function of parameter $\alpha = b_{\rm k}/n_{\rm x}t$, which effectively corresponds to strand DP $n_{\rm x}$ ($G_{\rm m} = 0.85k_{\rm B}T/\sigma^3$). The dashed line is the best fit to the equation

y=0.143x-0.00041. The inset shows the dependence of the calculated DP of network strands, $n_{x,{\rm calc}}=b_K/l\alpha$, on the strands' actual DP. The error bars are smaller than the symbol size and calculated by using fitting errors in **a. c**, Dependence of the loop coefficient $C_{{\rm loop}}$ on the average crosslink functionality $\langle f \rangle$ for linear chain networks (filled rhombs) and for diamond networks of end-linked chains with $n_x=150$ and a different density of dangling ends (filled circles). Note that the large value of $C_{{\rm loop}}$ for diamond networks follows from its definition (equation (3)). For perfect diamond networks with f=4, $C_{{\rm loop}}=2$, since the ratio $Gb_K/G_m\beta l=1$ (Supplementary Table 1).

Figure 2 outlines the essential steps of the forensic approach in application to a set of phantom networks with different crosslink densities. First, structural shear modulus G and strand extensibility parameter β are determined for each network by fitting their corresponding stress-elongation curves to equation (1) (Fig. 2a and Supplementary Fig. 1a). Second, we numerically solve equation (2) for α , which yields the DP of network strands as $n_{x,\text{calc}} = b_k/l\alpha$ within 8% of the actual n_x (inset in Fig. 2b), using the value of $b_k/l = 2.92$ known for model phantom networks (Supplementary Information). Third, we use the determined α and β to rewrite equation (3) as

$$G = G_{\rm m} \frac{\beta}{\alpha} \left(1 - \frac{2}{\langle f \rangle} \right) C_{\rm loop} \left(\frac{l}{b_{\rm K}} \alpha - \frac{1}{N} \right). \tag{4}$$

Plotting the reduced shear modulus $G\alpha/G_m\beta$ as a function of α enables the extracting of the structural parameters $\langle f \rangle$, C_{loop} and N from the slope and intercept (Fig. 2b). Specifically, we obtain $(1-2/\langle f \rangle)C_{\text{loop}} \approx 0.40 \pm 0.01$ and the DP of precursor chains $N_{\text{calc}} = 998$, which is close to the actual value 1,025. Finally, the obtained n_x and N are used to calculate $\langle f \rangle$ (Supplementary Equation (5)) and plot $C_{\text{loop}}(\langle f \rangle)$ (Fig. 2c). This results in C_{loop} being a decreasing function of $\langle f \rangle$. Note that the calculated C_{loop} includes contributions from all types of loops as well as higher order corrections due to dangling ends that are omitted in the analytical calculations of the loop factor 8,24 .

A similar analysis can be applied to diamond networks of end-crosslinked phantom strands with a varying density of dangling ends (inset in Fig. 2c, Supplementary Fig. 1c and Supplementary Table 1). A perfect diamond network without dangling chains has crosslink functionality f = 4 and can be viewed as a hierarchical system of loops with $C_{loop} = 2$ (Fig. 2c). Dangles lead to a decrease of average $\langle f \rangle$ and increase of C_{loop} , which scales inversely with $\langle f \rangle$. The inverse correlation reflects the slower decrease of the ratio $Gb_{\kappa}/G_{m}\beta l$, characterizing the network topology (network quality factor as defined below), in comparison with changes in $\langle f \rangle$ and the fraction of the repeat units n_x/N in dangling ends (equation (3)), pointing out the repartitioning of contributions from different network structural elements. Thus, the forensic approach executed on model networks provides complete information about the DP between crosslinks and effective crosslink functionality, and also quantifies the effect of loops and dangling ends on the network elasticity.

The stress–strain analysis becomes more complex for real networks with trapped entanglements, described by the following nonlinear equation of state 3,23 introduced in the spirit of the Mooney–Rivlin formulation of network elasticity 1,22

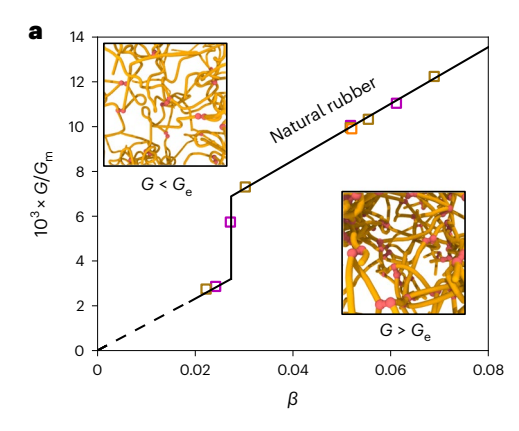
$$\sigma_{\text{true}}\left(\lambda\right) = (\lambda^2 - \lambda^{-1}) \left(\frac{G_e}{\lambda} + \frac{G}{3} \left[1 + 2 \left(1 - \frac{\beta(\lambda^2 + 2\lambda^{-1})}{3} \right)^{-2} \right] \right) \tag{5}$$

where $G_{\rm e}$ represents both the direct contributions of entanglements and indirect effect of crosslinks on stress support by entanglements. The entanglement term corresponds to a different mode of network deformation associated with the ability of entanglements to slide, redistributing the stress^{1,22}. This feature distinguishes entanglements from chemical crosslinks. In addition, entanglements cause an indirect effect on the structural modulus as

$$G = G_{\rm m} \frac{\beta}{\alpha} \left(1 - \frac{2}{f} \right) \left(\frac{l}{b_{\rm K}} \alpha + \frac{1}{N_{\rm eff}} \right) \tag{6}$$

where C_{loop} is absorbed by N_{effr} , which describes the partitioning of repeat units between stress-supporting structural elements (networks strands, entanglement strands and loops) and stress-free elements (dangling ends), and together with the sign in front of it, reflects the interplay between the different contributions. In contrast to equations (3) and (4), the sign '+' indicates that entanglements enhance stiffness by overpowering the contributions from dangles and loops. Unlike model networks with specific incorporated defects and the ones discussed previously, the partitioning representation is more adequate for real networks given the unfeasibility of separating individual contributions from specific elements of unknown network topology. Furthermore, this approach has proven to be instrumental in elucidating the interplay of entanglements and chemical crosslinks as well as evaluating the Kuhn length, as discussed in the following.

We apply equations (5) and (6) to establish the evolution of the mechanical properties of natural rubber upon increasing the crosslink density (Supplementary Figs. 4 and 5 and Supplementary Table 2)¹⁹. Two distinct deformation regimes with $G < G_e$ and $G > G_e$ separated by a sharp transition at $\beta \approx \alpha = 0.027$ were identified (Fig. 3a). From the slope value a = 0.13 at $\beta > 0.027$ and the known $b_k/l = 1.89$ and f = 4,



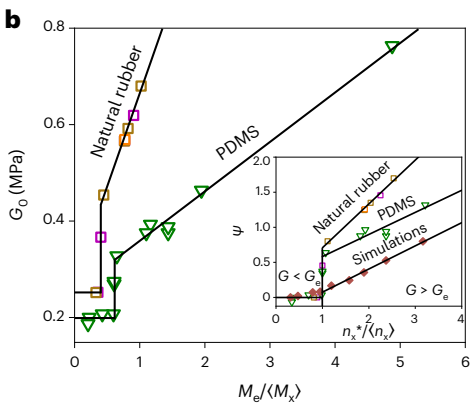


Fig. 3 | **Elasticity and percolation transition. a**, Evolution of the reduced structural shear modulus $G/G_{\rm m}$ with the firmness parameter β for natural rubber crosslinked in a melt of chains with number-averaged molecular mass $M_{\rm n}=195~{\rm kg~mol^{-1}}$ at $25~{\rm ^{\circ}C}$ ($f=4~{\rm and}~G_{\rm m}=33.16~{\rm MPa}$). The solid line corresponds to the equation $G/G_{\rm m}=0.5(\frac{n_{\rm x}(\alpha)}{\langle n_{\rm x}\rangle} \frac{l}{\langle b_{\rm k}\rangle}\beta+\frac{1}{N_{\rm eff}})=0.13\beta+0.0033$, for $\beta>0.027$.

The factor $n_x(\alpha)/\langle n_x \rangle \approx 2$ accounts for the renormalization of the DP of network strands due to effects of strand polydispersity (Supplementary Equations (10)–(15)). The solid-to-dashed line in the interval β < 0.027 indicates the extrapolation to infinitely long strands with $\beta = 0$. The insets show computer simulation snapshots for entanglement-controlled ($G < G_e$) and crosslink-controlled $(G > G_e)$ networks. **b**, Shear modulus at small deformations $G_0 \equiv \frac{1}{3} (\partial \sigma / \partial \lambda)_{\lambda=1} = G_e + G(1 + 2(1 - \beta)^{-2})/3$ as a function of the ratio $M_e / \langle M_x \rangle$ for randomly crosslinked natural rubber and tetrafunctional PDMS networks of end-crosslinked chains of different molecular weights. In PDMS networks, the number-averaged strand mass $\langle M_x \rangle$ varies between 2,460 and 58,000 g mol⁻¹, while the entanglement molecular weight in a PDMS melt is $M_e = 12,000 \,\mathrm{g}$ mol⁻¹. Solid lines show general trends. The inset shows the normalized shear modulus $\Psi = (G_0 - G_{av})/G_{av}$ versus the ratio $n_v^*/\langle n_v \rangle$ for different networks, as indicated. The coarse-grained networks studied in computer simulations are made by crosslinking chains with DP = 1,025 in a melt (filled rhombs; Supplementary Fig. 2 and Supplementary Table 1). Shear modulus G_{av} corresponds to the average value in the plateau regime, and n_x^* defines the location of the percolation transition. The sharpness of the transition is a general feature for all networks studied experimentally. However, in computer simulations, the sharp transition transforms into a crossover, for which there could be several explanations, as discussed at the end of Supplementary Section 5.

we estimate $\langle n_x \rangle = n_x^* = 0.5/a\beta \approx 143$, which corresponds to the transition at $\beta = 0.027$ and accounts for strand polydispersity (Supplementary Equations (10)–(15)). Since transition n_x^* is larger than the entanglement DP in a melt of precursor chains $n_e \approx 57$ (ref. 25), we argue that there is a percolation-like transition²⁶ between the two types of networks, where elasticity is controlled by either crosslinks ($\langle n_x \rangle < n_x^*$) or entanglements ($\langle n_x \rangle > n_x^*$; insets in Fig. 3a). In these networks, the entanglement contributions (before and after n_x^*) are qualitatively different, which results in the stepwise G increase, change of

its functional form (Fig. 3a) and non-monotonic dependence of the entanglement modulus on $\langle n_x \rangle$ (Supplementary Figs. 5b and 2b), Specifically, this transition highlights two different mechanisms of entanglement response to deformation. In densely crosslinked networks $(\langle n_x \rangle < n_x^*)$, the increase of the G and G_e (Supplementary Fig. 5b) moduli with increasing crosslinking density is due to a decrease of entanglements in dangling ends combined with an enhancement of the constraints imposed on entanglement fluctuations. In weakly crosslinked networks $(\langle n_x \rangle > n_x^*)$, these constraints are relaxed, and fluctuations of entanglements are controlled by a soft confining potential like in a melt of uncrosslinked chains. With increasing $\langle n_x \rangle$, the entanglement modulus G_e monotonically increases towards the melt plateau value (Supplementary Figs. 5b and 2b), while the structural modulus decreases towards zero (Fig. 3a and Supplementary Table 1). This also explains why networks with $\langle n_x \rangle \approx n_e$ have an entanglement modulus smaller than that in a melt of precursor chains.

The existence of the transition is further corroborated by the dependence of the shear modulus at small deformations (G_0) on the ratio $n_e/\langle n_x \rangle$ for natural rubber and tetrafunctional (f=4) networks of end-crosslinked PDMS chains (Supplementary Fig. 6, Supplementary Table 3 and Fig. 3b)⁷. Even though the networks differ in both chemistry and topology, they demonstrate the same percolation behaviour during a crosslinking process: a sharp increase in shear modulus at $\langle n_x \rangle = n_x^*$ followed by a linear increase of modulus for $\langle n_x \rangle < n_x^*$. In the entanglement-controlled regime, $n_x^* < \langle n_x \rangle$, the plateau modulus of the PDMS networks is close to that of an entangled linear PDMS melt $(G_e = 0.2 \text{ MPa})$. By contrast, the majority of the natural rubber samples are softer than $G_e = 0.58$ MPa (ref. 25), which suggests a dilution of entanglements during the network formation. We observed no evidence that would suggest a disruption of the network structure at low crosslinking densities or explain the modulus drop. This finding calls into question the commonly held belief of continuous crossover between two types of networks^{6,22} and should be a subject of future research.

Finally, we illustrate the applicability of the forensic approach to networks with brush-like strands where stress-supporting backbones are diluted by side chains with DP = n_{sc} separated by n_{g} backbone repeat units as defined by a dilution factor $\varphi = n_g/(n_g + n_{sc})$ (inset, Fig. 4a). As for the linear chain networks with $n_{sc} = 0$ ($\varphi = 1$; Fig. 2a), the forensics procedure begins with fitting experimental stress-elongation curves (Fig. 4a) with equation (5) to obtain G and B values (Supplementary Figs. 7–13 and Supplementary Table 4). The Kuhn length b_{κ} of the brush backbone is determined from the slope of the reduced structural shear modulus $G\alpha/G_m\beta\varphi$ as a function of α (Fig. 4b). For systems with a lower grafting density (linear and comb-like networks), several parallel lines are observed with slopes equal to $(1 - 2/f)l/b_K$, which is consistent with the fact that b_{κ} is not affected by loosely grafted side chains. The vertical shift between the lines reflects changes in the fraction of repeat units belonging to stress-supporting strands characterized by $N_{\rm eff}$, including the contribution from trapped entanglements. The Kuhn length of linear and comb-like PBA chains (f = 4) is revealed to be $b_K = b = 1.91$ nm, which is in excellent agreement with literature values b = 1.79 - 1.90 nm of the bare PBA backbone²⁷.

In densely grafted bottlebrush networks, the inverse relationship observed between slope and grafting density is due to steric repulsion between side chains, resulting in backbone extension and stiffening (Fig. 4b). Plotting the normalized Kuhn length $b_{\rm K}/b$ as a function of the so-called crowding parameter Φ demonstrates the effect of side chains on strand stiffness, where Φ describes the degree of interpenetration of side chains belonging to different brush molecules (Fig. 4c)^{28,29}. In the comb regime ($\Phi < \Phi^* \approx 0.7$), the steric repulsion between side chains is weak and the effective Kuhn length of the backbone is $b_{\rm K} \approx b$ (refs. 28,29). However, in bottlebrush systems ($\Phi > \Phi^*$), the repulsion between densely grafted side chains results in backbone stiffening as $b_{\rm K} \approx b\Phi/\Phi^*$ (refs. 29,30). This behaviour is universal as it was observed

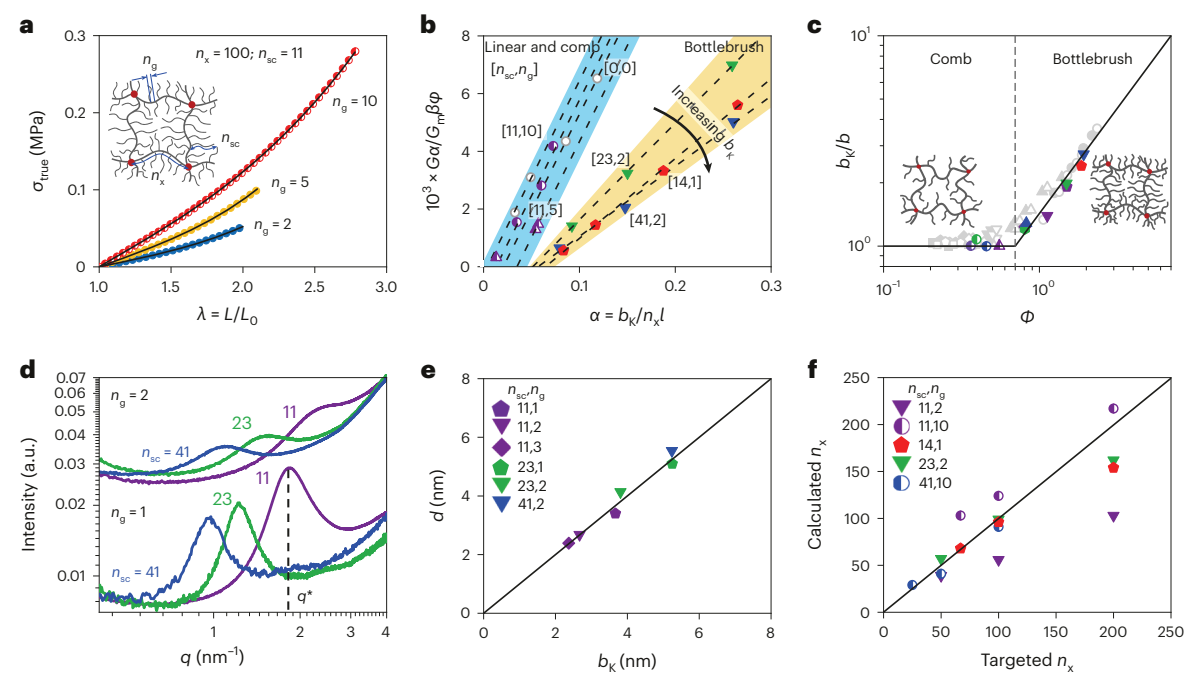


Fig. 4 | **Forensics of brush network elasticity. a**, Stress-elongation curves measured upon uniaxial extension of PBA brush elastomers with different grafting densities, as indicated. Solid lines are the best fits to equation (5) by considering G_e , G and G as fitting parameters (Supplementary Figs. 7–13 and Supplementary Table 4). **b**, The reduced structural shear modulus described by $\frac{G\alpha}{Gm\beta\phi} = (1-\frac{2}{f})(\frac{l}{b_K}\alpha - \frac{1}{N_{\rm eff}})$ is plotted versus parameter G for linear and comb (blue region) and bottlebrush (yellow region) PBA networks (G = 4 and G = 20.83 MPa). Unlike entangled linear chain networks (equation (6)), the sign '-' in front of the G 1/N_{eff} term indicates suppression of entanglements in brush networks. The dashed lines are the best fits to the equation G = G = G where the slope G and intercept G give G is and G = G pairs for networks with PBA linear strands, (0.067,0.0014), [0,0] and (0.067,0.0002), [0,0]; PBA comb strands,

(0.067,0.0023), [11,5] and (0.066,0.0009), [11,10]; PBA bottlebrush strands, (0.033,0.0017), [23,2] and (0.024,0.0014), [41,2]; and PDMS bottlebrush strands, (0.027,0.0022), [14,1]. **c**, The reduced Kuhn length, $b_{\rm K}/b$, as a function of the crowding parameter, $\Phi = \phi^{-1} n_{\rm sc}^{-1/2}/\rho(b1)^{3/2}$ for PBA and PDMS brush polymers as well as computer simulation data (grey symbols) 29,30 . The vertical dashed line shows the crossover between the comb and bottlebrush regimes at $\Phi = \Phi^* \cong 0.7$ (refs. 29,30). The legend for the symbols is given in Supplementary Table 4. **d**, Small-angle X-ray scattering intensity curves as a function of the scattering vector q for PBA brush networks at fixed targeted $n_{\rm x}=100$ with $n_{\rm g}=1, n_{\rm g}=2$ and various DPs of side chains, $n_{\rm sc}$, q^* corresponds to the scattering vector at the peak position and a.u. denotes arbitrary units. **e**, Correlation between bottlebrush diameter $d=2\pi/q^*$ calculated from q^* in **d** and Kuhn length $b_{\rm K}$ obtained from forensic analysis. **f**, Correlation between the targeted DP crosslinks and ones calculated by using the forensic approach.

for brush elastomers with different side chains (PBA, PDMS) 20,21 as well as in molecular dynamics simulations of bottlebrush melts, providing evidence of (chemical) universality (Fig. 4c) 29,30 . The obtained $b_{\rm K}$ values were compared with the distance between adjacent brush backbones, where the intrinsic contrast of electron density at the backbone results in a distinct scattering peak corresponding to the brush diameter, $d = 2\pi/q^*$ where q^* is a location of the peak in scattering function (Fig. 4d) 21,31 . The excellent agreement between the bottlebrush diameter d and the Kuhn length derived from the forensic approach (Fig. 4e) is consistent with analytical calculations and computer simulations of b_K in bottlebrush melts 28,32 .

Following the forensic protocol outlined previously in this paper, we use the Kuhn length $b_{\rm K}$ and value of parameter α to calculate the DP between crosslinks, $n_{\rm x,calc}=b_{\rm K}/l\alpha$ (Supplementary Table 4). The obtained $n_{\rm x,calc}$ scales linearly with targeted $n_{\rm x}$, which corroborates the self-similarity of the synthesized networks (Fig. 4f). The deviation in absolute numbers between the targeted and true $n_{\rm x}$ values is ascribed to the inevitable variations in the synthetic conditions between individual series, which in turn influences the crosslinking efficiency.

Varying network topologies results in different patterns of stress distribution between structural elements. To quantify a network's effectiveness in absorbing an applied force, we introduce a quality factor, κ , defined as the ratio of the real network modulus G to the defect-free affine network model, $G_{\rm affine}$, in which stress is evenly divided between all network strands^{1,22}

$$\kappa = \frac{G}{G_{\text{affine}}} = \frac{Gb_{\text{K}}}{G_{\text{m}}\beta l} \tag{7}$$

which reduces to $\kappa = Gn_x/G_m$ for networks of linear flexible chains. This parameter is directly related to the topology of the stress-supporting scaffold (equations (3) and (6)) and depends on strand flexibility (Supplementary Equations (17)–(21)). To account for b_{κ} variation in linear, brush-like, covalent and self-assembled networks, it is convenient to plot the quality factor as a function of the number of Kuhn segments per network strand $\alpha^{-1} \equiv n_x l/b_K$, to elucidate the variation of network quality with strands of different flexibility (Fig. 5). For defect-free unentangled diamond networks, prepared by the end-crosslinking of identical chains³³, $\kappa = 1$, indicating a uniform stress distribution independent of n_x . In real networks such as natural rubber¹⁹, the reduction in stress-supporting strands results in κ < 1. Furthermore, the entangled networks first demonstrate an upward trend followed by a downward trend at $\alpha^{-1} \cong 70$ ($n_{x,calc} = 143$), which is ascribed to a transition to the entanglement-controlled network elasticity (Supplementary Table 2). Further reduction of κ is observed for networks with comb-like strands²⁰ due to a considerable fraction of stress-free side chains and dangling ends (Supplementary Table 4). In bottlebrush networks (Supplementary Table 4)20, the increase of grafting density leads to an additional decrease of κ between 0.01 and 0.1 due to the stiffening of the brush strands by steric repulsion between densely

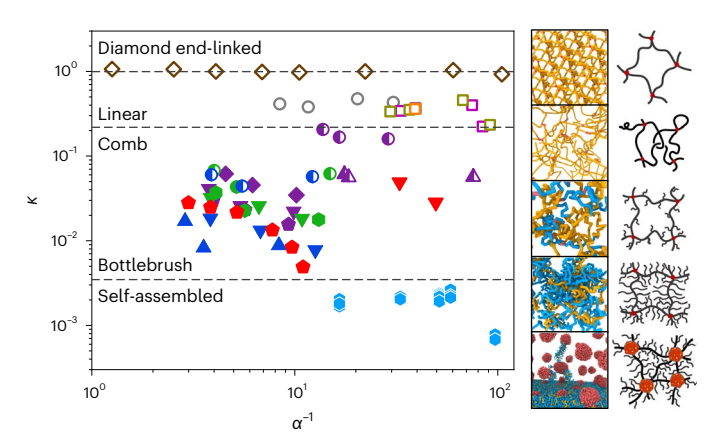


Fig. 5 | **Network topology classification.** Mapping of polymer networks with different topologies in terms of quality factor κ and number of Kuhn segments per network strand, $\alpha^{-1} \equiv n_x l/\beta_\kappa$. The analysed networks include end-crosslinked diamond networks studied in computer simulations (open rhombs), natural rubber (open squares), networks of comb strands (half-filled symbols) and bottlebrush strands (filled symbols) and a self-assembled network of linear–bottlebrush–linear (PMMA–PDMS–PMMA) block copolymers (filled blue hexagons); poly(methyl methacrylate) (PMMA). Legends for other symbols are given in Supplementary Tables 4 and 5. The pictures on the right show computer simulation snapshots of the three-dimensional network structure and schematics of the network mesh.

grafted side chains. For networks of comb and bottlebrush strands with identical φ , the quality factor decreases with increasing α^{-1} , indicating an increase in the density of network defects with increasing DP of the strands. For self-assembled networks of linear–bottlebrush–linear block copolymers²¹, the quality factor falls below the covalent brush networks (Supplementary Table 5). The worsening of the stress distribution in such networks is a result of stronger stretching of stress-supporting bottlebrush strands and their substantial dilution by bulky network nodes formed upon the self-assembly of the linear end blocks. The data are separated into two groups of κ values, corresponding to the spherical or cylindrical morphology of the linear block domains.

To summarize, we presented a forensic methodology for decoding the DP of stress-supporting strands, strand flexibility (Kuhn length) and network topology by analysing the nonlinear response of elastomers to deformation. The introduction of the quality factor, κ , established a universal classification of self-assembled and chemical networks made of strands with different molecular architectures according to the stress distribution between network structural elements. For natural rubber and PDMS networks, we discovered a percolation transition between networks with crosslink- and entanglement-controlled elasticity. Application of this technique to networks with brush-like strands elucidated the dependence of the Kuhn length on the brush molecular architecture. Future development of the forensic approach could transform it into a valuable technique for the characterization of more-complex synthetic and biological networks and gels³⁴ due to its combination of simplicity and comprehensive explanatory power⁵, for the accurate prediction of their structures 3,4,34-36. Furthermore, decoding the structure of real networks is crucial for the verification of architectural codes generated by future artificial intelligence machinery in soft matter design. By comparing the artificial-intelligence-recommended and as-synthesized architectural codes, one will be able to optimize the synthesis conditions to achieve optimal mechanical properties.

Online content

Any methods, additional references, Nature Portfolio reporting summaries, source data, extended data, supplementary information, acknowledgements, peer review information; details of author contributions

and competing interests; and statements of data and code availability are available at https://doi.org/10.1038/s41563-023-01663-5.

References

- Treloar, L. R. G. The Physics of Rubber Elasticity (Clarendon Press, 1975).
- Flory, P. J. Principles of Polymer Chemistry (Cornell Univ. Press. 1971).
- 3. Sheiko, S. S. & Dobrynin, A. V. Architectural code for rubber elasticity: from supersoft to superfirm materials. *Macromolecules* **52**, 7531–7546 (2019).
- McKenna, G. B. Soft matter: rubber and networks. Rep. Prog. Phys. 81, 0666602 (2018).
- Danielsen, S. P. O. et al. Molecular characterization of polymer networks. Chem. Rev. 121, 5042–5092 (2021).
- Dossin, L. M. & Graessley, W. W. Rubber elasticity and well-characterized polybutadiene networks. *Macromolecules* 12, 123–130 (1979).
- Patel, S. K., Malone, S., Cohen, C., Gillmor, J. R. & Colby, R. H. Elastic-modulus and equilibrium swelling of poly(dimethylsiloxane) networks. *Macromolecules* 25, 5241–5251 (1992).
- Zhong, M., Wang, R., Kawamoto, K., Olsen, B. D. & Johnson, J. A. Quantifying the impact of molecular defects on polymer network elasticity. Science 353, 1264–1268 (2016).
- Chase, W., Lang, M., Sommer, J.-U. & Saalwächter, K. Cross-link density estimation of PDMS networks with precise consideration of networks defects. *Macromolecules* 45, 899–912 (2012).
- Chasse, W., Lang, M., Sommer, J.-U. & Saalwächter, K. Correction to cross-link density estimation of PDMS networks with precise consideration of networks defects. *Macromolecules* 48, 1267–1268 (2015).
- Smith, S. B., Cui, Y. J. & Bustamante, C. Overstretching B-DNA: the elastic response of individual double-stranded and single-stranded DNA molecules. Science 271, 795–799 (1996).
- Neuman, K. C., Lionnet, T. & Allemand, J. F. Single-molecule micromanipulation techniques. *Ann. Rev. Mater. Res.* 37, 33–67 (2007).
- 13. Flory, P. J. Network topology and the theory of rubber elasticity. *Br. Polym. J.* **17**, 96–102 (1985).
- Langley, N. R. Elasticity effective strand density in polymer networks. Macromolecules 1, 348–352 (1968).
- Miller, D. R. & Macosko, C. W. New derivation of post gel properties of network polymers. *Macromolecules* 9, 206–211 (1976).
- Sandakov, G. I., Smirnov, L. P., Sosikov, A. I., Summanen, K. T. & Volkova, N. N. NMR analysis of distribution of chain lengths between crosslinks of polymer networks. *J. Polym. Sci. Polym. Phys.* 32, 1585–1592 (1994).
- 17. Bastide, J. & Candau, S. J. in *Physical Properties of Polymeric Gels* (ed. Cohen, J. P.) 143–308 (Wiley, 1996).
- Edwards, S. F. & Vilgis, T. A. The tube model theory of rubber elasticity. Rep. Prog. Phys. 51, 243–297 (1988).
- Mullins, L. Determination of degree of crosslinking in natural rubber vulcanizates. Part IV. Stress-strain behavior at large extensions. J. Appl. Polym. Sci. 2, 257–263 (1959).
- Vatankhah-Varnosfaderani, M. et al. Mimicking biological stress-strain behaviour with synthetic elastomers. *Nature* 549, 497–501 (2017).
- Vatankhah-Varnosfaderani, M. et al. Chameleon-like elastomers with molecularly encoded strain-adaptive stiffening and coloration. Science 359, 1509–1513 (2018).
- 22. Rubinstein, M. & Colby, R. H. *Polymer Physics* (Oxford Univ. Press, 2003).
- Dobrynin, A. V. & Carrillo, J.-M. Y. Universality in nonlinear elasticity of biological and polymeric networks and gels. *Macromolecules* 44, 140–146 (2011).

- Panyukov, S. Loops in polymer networks. *Macromolecules* 52, 4145–4153 (2019).
- Fetters, L. J., Lohse, D. J. & Colby, R. H. in Physical Properties of Polymers Handbook (ed. Mark, J. E.) 445–452 (Springer, 2007).
- 26. Staufer, D. *Introduction to Percolation Theory* (Taylor and Francis, 1985).
- Ahmad, N. M., Lovell, P. A. & Underwood, S. M. Viscoelastic properties of branched polyacrylate melts. *Polym. Int.* 50, 625–634 (2001).
- Daniel, W. F. M. et al. Solvent-free, supersoft and superelastic bottlebrush melts and networks. Nat. Mater. 15, 183–189 (2016).
- Liang, H., Cao, Z., Wang, Z., Sheiko, S. S. & Dobrynin, A. V. Combs and bottlebrushes in a melt. *Macromolecules* 50, 3430–3437 (2017).
- Liang, H., Wang, Z., Sheiko, S. S. & Dobrynin, A. V. Comb and bottlebrush graft copolymers in a melt. *Macromolecules* 52, 3942–3950 (2019).
- 31. Maw, M. et al. Brush architecture and network elasticity: path to the design of mechanically diverse elastomers. *Macromolecules* **55**, 2940–2951 (2022).
- 32. Cao, Z., Carrillo, J.-M. Y., Sheiko, S. S. & Dobrynin, A. V. Computer simulations of bottle brushes: from melts to soft networks. *Macromolecules* **48**, 5006–5015 (2015).

- Carrillo, J.-M. Y., MacKintosh, F. C. & Dobrynin, A. V. Nonlinear elasticity: from single chain to networks and gels. *Macromolecules* 46, 3679–3692 (2013).
- 34. Peak, C. W., Wilker, J. J. & Schmidt, G. A review on tougth and sticky hydrogels. *Colloid Polym. Sci.* **291**, 2031–2047 (2013).
- 35. Zhang, Y. S. & Khademhosseini, A. Advances in engineering hydrogels. *Science* **356**, eaaf3627 (2017).
- 36. Peppas, N. A., Hilt, J. Z., Khademhosseini, A. & Langer, R. Hydrogels in biology and medicine: from molecular principles to bionanotechnology. *Adv. Mater.* **18**, 1345–1360 (2006).

Publisher's note Springer Nature remains neutral with regard to jurisdictional claims in published maps and institutional affiliations.

Springer Nature or its licensor (e.g. a society or other partner) holds exclusive rights to this article under a publishing agreement with the author(s) or other rightsholder(s); author self-archiving of the accepted manuscript version of this article is solely governed by the terms of such publishing agreement and applicable law.

@ The Author(s), under exclusive licence to Springer Nature Limited 2023

Methods

Computer simulations

Coarse-grained molecular dynamics simulations of entangled and phantom networks were performed using the Large-scale Atomic/Molecular Massively Parallel Simulator. Network strands were modelled as bead-spring chains of beads interacting through the truncated and shifted Lennard-Jones potential and connected by the finite extensible nonlinear elastic bonds. The same finite extensible nonlinear elastic bonds were used for crosslinks. In addition, the chain bending rigidity was introduced by imposing an angular potential between two neighbouring unit bond vectors. We studied phantom and entangled networks of linear chains and diamond networks of phantom linear strands. Networks were deformed uniaxially at a constant volume and temperature under three-dimensional periodic boundary conditions. The true stress was calculated from the pressure tensor.

Nuclear magnetic resonance spectroscopy

Conversion of macromonomers was determined from 1H NMR spectra recorded on a Bruker NMR spectrometer operating at 400 MHz for 1H (Bruker AVANCE III Nanobay 400 MHz). MestReNova v.14.1.0-24037 software (Mestrelab Research) was used to analyse the NMR spectra.

Mechanical properties

The mechanical properties for all samples were determined from uniaxial tensile testing using an RSA-G2 dynamic mechanical analyser (TA Instruments) at 22 °C. Samples were cut into dog-bone shapes with a bridge of dimensions 2 mm \times 1 mm \times 12 mm and measured at room temperature and a strain rate of 0.005 s⁻¹ corresponding to the elastic plateau identified by frequency sweeps. True stress $\sigma_{\rm true}$ versus elongation ratio λ curves were fitted with equation (5) to extract G, $G_{\rm e}$ and β .

Rheology

Frequency sweeps were performed on the ARES-G2 rheometer (TA Instruments) with 8 mm compression plate geometries. Samples were prepared by cutting 8-mm-diameter discs with an approximate height of 1 mm (exact height was specified in the rheometer for each sample). The frequency sweep was performed from 0.01 to 100 Hz at 22 °C with a strain of ε = 0.05.

X-ray scattering

Small-angle and medium-angle X-ray scattering was conducted at the IDO2 beamline of the European Synchrotron Radiation Facility in Grenoble, France. In the experiments, a photon energy of 12.46 keV was used. The incident monochromatic X-ray beam was collimated to a footprint on the sample of $100 \times 200 \ \mu m^2$. The total photon flux was estimated to be 9×10^{11} photons s⁻¹, allowing for exposures of -100 ms. A Rayonix MX-170HS installed inside a motorized wagon that travels in a 35-m-long vacuum flight tube was employed for the recording of scattering intensities at a sample-to-detector distance of 1.5 m. For optimization of the scattering signal, binning of 2×2 pixels was applied, resulting in an effective pixel size of 89 μ m in both directions.

The two-dimensional data recorded in transmission were preliminarily corrected, calibrated and reduced to one dimension by using the small-angle X-ray scattering utilities platform.

Data availability

All data supporting the findings are provided as figures and accompanying tables in the article and Supplementary Information. Data files for all figures are available from the corresponding authors on request.

Acknowledgements

This work was supported by the National Science Foundation under grants DMR 1921835 (S.S.S., M.M.), DMR 1921923 (A.V.D., M.J.), DMR 2049518 (A.V.D., Y.T., M.J.) and DMR 2004048 (S.S.S., F.V.). E.A.N. and D.A.I. acknowledge the Ministry of Science and Higher Education of the Russian Federation for financial support in the frame of state contract no. 075-15-2022-1117 from June 30, 2022. A.V.D. and S.S.S. are grateful to E. Samulski for the critical reading of the manuscript and numerous stimulating discussions. We acknowledge the contribution of B. J. Morgan and A. N. Keith to the synthesis of well-defined PBA elastomers and linear–bottlebrush–linear copolymers, reported previously. E.A.N. and D.A.I. acknowledge the European Synchrotron Radiation Facility for provision of synchrotron beamtime at the IDO2 beamline and thank the staff of the European Synchrotron Radiation Facility and E. A. Bersenev for assistance.

Author contributions

A.V.D. developed the concept and theoretical foundation; F.V. and M.M. performed the synthesis, characterization and mechanical testing of brush networks; Y.T. analysed correlations between the network structure and mechanical properties; M.J. and Y.T. performed molecular dynamics simulations of polymer networks and analysed their properties; E.A.N. and D.A.I. performed X-ray scattering measurements; and A.V.D. and S.S.S. were the primary writers of the manuscript and the principal investigators. All authors discussed the results and provided feedback on the manuscript.

Competing interests

The authors declare no competing interests.

Additional information

Supplementary information The online version contains supplementary material available at https://doi.org/10.1038/s41563-023-01663-5.

Correspondence and requests for materials should be addressed to Andrey V. Dobrynin or Sergei S. Sheiko.

Peer review information *Nature Materials* thanks the anonymous reviewers for their contribution to the peer review of this work.

Reprints and permissions information is available at www.nature.com/reprints.